Investigation on temperature-dependent structural, dielectric and impedance characteristics of Cu-doped CaFe$_x$Ti$_{1-x}$O$_{3-\delta}$ nanotitanates

Mathu Sridharpanday[1], Ramasubramanian Brindha[1], Murugan Vinoth[1], Kandhasamy Narthana[1], and Venkatachalam Rajendran[1,2,*] (ID)

[1] *Centre for Nano Science and Technology, K.S Rangasamy College of Technology, Tiruchengode 637215, India*
[2] *Centre for Nano Science and Technology, Dr. N.G.P. Arts and Science College, Coimbatore 641048, India*

ABSTRACT

In recent days, the development of low-cost, sustainable, efficient electrode materials for energy storage applications is of great interest. Herewith, Cu-doped Ca(Ti$_{0.9}$Fe$_{0.1}$)O$_{3-\delta}$ (Cu:CTF) double-perovskite electroceramic, heat-treated at diverse temperatures (800–1100 °C) were prepared using sol–gel technology. X-ray diffraction pattern confirmed the orthorhombic structure of the prepared Cu:CTF perovskites. Significant traces of TiO$_2$, CuO vanishes at elevated temperatures, which is evident from the XRD pattern. Further, the secondary phase traces were also observed in XRD, but without changing its crystal structure of Cu:CTF nanotitanate. The crystalline nature of the Cu:CTF ceramic was identified around 750 °C employing TG/DTA. UV–visible spectroscopy demonstrates the poor visible absorbance region towards the red shift with the bandgap variation of 5.28–5.42 eV. The nature of the Cu:CTF particles were analyzed using electron microscopes with the estimated particle size between 52 and 190 nm. Considering the action of temperature and frequency, complex impedance spectroscopy was utilized to analyse the inter- and intra-grain inclusions. Complex impedance spectroscopy study confirms the existence of dipole–dipole relaxation and Maxwell–Wagner (MW) polarisation for the samples heated above 900 °C. However, the a.c. test reveals the presence of conduction due to the addition of Cu^{2+} ions to CaTi$_{1-x}$Fe$_x$O$_{3-\delta}$ perovskite, which enhances oxygen vacancies and is strongly dependent on the inhibition of the hopping conduction mechanism.

Address correspondence to E-mail: veerajendran@gmail.com; vrajendran@drngpasc.ac.in

1 Introduction

Developing an eco-friendly, low cost and sustainable energy technology is the key motto of modern-day researchers. It is essential to note that the most needed alteration of this twenty-first century relies on renewable and sustainable energy technologies adapted for power generation and transportation. Fuel demand has been escalating in proportion to the growing population for decades. While considering various types of power-generation, Fuel cells (FC) seems to be the best alternate, owing to clean, efficient and eco-friendly technology, which can be even functionalized with hydrocarbons [1–3]. Notably, Solid Oxide Fuel Cell (SOFC), discharges water as a half-cell reaction product and consumes O^{2-} ions from the enclosed surrounding. Furthermore, the electrolyte and electrodes are preferably in solid-state because of the high temperature requirement for the motion of the electrons [4]. On the other hand, high temperature reversible reactions, low internal resistances of the reactive component, facilitates the burning of toxic substances (such as CO, CO_2, sulphur, etc.) and creates many potential benefits, including utilization of waste heat for fuel reformation [5, 6].

Over the past few decades, Mixed Ionic-Electronic Conductor (MIEC) has been extensively used due to its potential benefits in fuel cells. Perovskite materials, particularly $CaBTiO_3$ (B = Fe, Ni, Ce, Zn, Co, etc.), $ACu_3Ti_4O_{12}$ (A = Ca, Sm, La, Gd, Y, etc.) and $LaCMnO_3$ (C = Sr, Na, K, Mg, P, etc.) are known for their intended structure, high surface reaction, high chemical and thermal stability [7]. Moreover, heterogeneous system of grains and grain boundary contribute to higher stability and performance which is evident through boundary layer capacitance (BLC) model. Here, the grain suppresses the electron transfer within the ohmic region due to polarisation losses. Consequences of polarization in the perovskite oxide materials were identified using complex impedance spectroscopy [8, 9]. Therefore, the development of perovskite materials with high oxygen vacancies through the modification of cation substituent will lead to the enhanced dynamics, superior Oxygen Reduction Reaction (ORR) and Hydrogen Evolution Reaction (HER) kinetics [10, 11].

Recently, the dielectric properties of $CaTi_{1-x}Fe_xO_{3-\delta}$ (CTF; x = 0.05 ≤ x ≤ 0.6) and $CaCu_3Ti_4O_{12}$ (CCTO) perovskites over a broad array of frequencies (100 kHz–1 MHz) at room temperature has been investigated by researchers. Moreover, the dielectric constants are identified in accordance with the temperature (< 327 °C) for CTF and CCTO such as $< 10^4$ and $< 10^5$, respectively, with grain sizes of 100 μm [12, 13]. Thermal expansion of ABO_3 type perovskites is similar to Yttria Stabilized Zirconia (YSZ) electrolytes which makes ABO_3 favourable with high electronic stability. However, efforts are being made to ensure that the requirements of SOFC technologies are satisfied such as high conductivity at low temperatures (600–800 °C). High conductivities are well demonstrated with MIECs. Beneficially, low temperature performance of SOFC reduces stability challenges in electrodes and electrolytes [14, 15].

Electrocatalysts and solid-state electrolytes plays a momentous role in MIEC, supporting fast ionic exchange mechanism without producing toxic greenhouse gases. However, at the nanoparticle level, the curvature and lattice displacement cause suspicious defects and vacancies in the crystalline array, owing to larger dielectric constant [16–18]. There are numerous in-depth reports on the conduction properties of MIEC perovskite materials, namely CTF and CCTO. From these two, the CTF system supports both electronic and ionic conductivity and has superior thermo-chemical stability towards high frequency dispersion phenomena such as, *thermally activated process* [19–21]. To improve the oxidation–reduction stability and electrical conductivity, the electrolytic polarization effects have to be minimized at the interfacial surfaces. Thereby, unsurpassed charge carrier transfer mechanism should be achieved. This can be done, using thin film or layered perovskite structure with high porosity as electrode and electrocatalysts materials [22, 23].

In this present study, the Cu-doped CTF nanotitanates were synthesized using the sol–gel technique with grain size in the sub-micrometric range. Further, the reduction of ohmic resistance at grain and grain boundaries as well as total feasible conductivities for Cu:CTF were measured in accordance with various sintering temperature. Thermal stability of, Cu:CTF at higher densities were examined.

2 Experimental procedure

Pure grade chemicals (Himedia, Merck, and Sigma-Aldrich; 99.0%;) were used for the synthesis without further alteration or purification employing *Sol–gel* methodology [24, 25]. The precursors were taken in stoichiometric ratios, to synthesize copper (Cu^{2+})-doped calcium iron titanate electroceramics. Initially, stoichiometric amounts of $Ca(OH)_2$ and $C_{12}H_{28}O_4Ti$ were mixed with 1:1 ratio in CH_3COOH and C_3H_8O, respectively, and stirred separately until the particles gets completely dissolved. The mixture was stirred at 20 °C for 20 min. Then, $Fe(NO_3)_3.9H_2O$ solution was taken in a stoichiometric ratio and was added to the above mixture under constant stirring. Later, $Cu(NO_3)_2$ salt of 0.55 mol% was dissolved in 20 mL of deionised water and was added to the solution in stirrer.

The obtained mixture of solutions was continuously stirred for 2 h at 25 °C. At this stage, ammonium hydroxide (NH_4OH) solution was added drop wise to maintain pH to ∼ 7. Then, the solution was kept inside an oven at an optimum temperature of 70 °C. After evaporation of water molecules, the suspended solution starts to solidify. Within a few minutes, the gel rapidly turns into a foam-like substance and flows from the top part of the beaker. The foam seemed to be light in weight, smooth and porous in nature. The sample was allowed to dry for some time and then was transferred to the muffle furnace for direct calcination at 700 °C for 6 h (hereafter can be also termed as Cu:CTF). The phase nature of the prepared perovskite material was achieved during the powder calcination. After cooling to optimal temperature, the calcined crystalline Cu:CTF perovskite was grinded for 15 min to obtain fine powders.

The calcined nanocrystalline perovskite was then old squashed into pellets using viscous gel (16% poly(vinyl alcohol) (PVA), 5% glycerine and 79% DD water) as binding agent, in hydraulic pellet press maker (KIMAYA Engineers, Maharashtra, India). The pressed pellets were in the dimensions of 13 mm diameter and 1.8 mm thickness. The pellets were sintered at four different temperatures such as 800 °C, 900 °C, 1000 °C, and 1100 °C for 8 h in atmospheric air. Hereafter the heated samples are termed as C8, C9, C10, and C11, respectively. After quenching at room temperature, all the sintered pellets were smoothly polished using silicon carbide

(SiC) sheet and high-grade silver paste (Ted Pele, USA) was adhered on both sides of the pellet to carry out electrical measurements [25]. The protocol for the preparation of Cu:CTF nanoperovskites is shown in Fig. 1.

Archimedes liquid displacement method was used to find out the density of prepared samples. To determine the theoretical density and mass of the sintered samples (ρ_{th}), we have used digital balance (Sartorius, Germany) employing the relation [26],

$$\rho_{th} = \frac{W_a}{W_a - W_b} \times \rho_p \tag{1}$$

Where W_a and W_b are mass of the sample in air and in buoyant respectively, and ρ_b is the density of the buoyant (CCl_4). The measurement was taken multiple times with different sizes of disks to maintain precision in the value of density. The percentage error in density measurement was found to be ± 0.05.

The ultimate aim of this work is to develop a potential supportive electrode material for SOFCs. For the identification of desired physical parameters, surface structures, particle size, shape and conductance, various characterization studies were performed. Percentage of mass loss and decomposition rates were recorded utilizing STA PT1600 TG/DTA licensed by (Robbinsville, NJ) with the operating temperature ranging from 27 to 1000 °C. X-ray powder diffraction (XRD) studies were carried out using an X'PERT-PRO diffractometer (X'Pert-Pro, PanAnalytical, USA) using Cu Kα as a radiation (λ = 1.54056 Å) source in an extensive range of diffraction angles i.e., 2θ ($10° \leq 2\theta \leq 80°$). The studies were recorded with the operating voltage of 40 kV, 35 mA current and scanning rate of 1° min^{-1}. Average crystallite size of synthesised nanotitanates was calculated using the Scherrer formula [27].

$$D = \frac{k\lambda}{\beta \cos \theta} \tag{2}$$

where D is the average crystallite size, k is the Scherrer's constant (k = 0.94), λ is the wavelength of X-rays, β is the Full peak Width at Half-Maximum (FWHM) or line broadening intensity in radians and θ is the Bragg's diffraction angle. Microstructural and morphology studies were investigated using Scanning Electron Microscope (SEM; JEOL JSM-6390A, Tokyo, Japan). The TEM (CM200; Philips, United States) was used to magnify the nanotitanates at
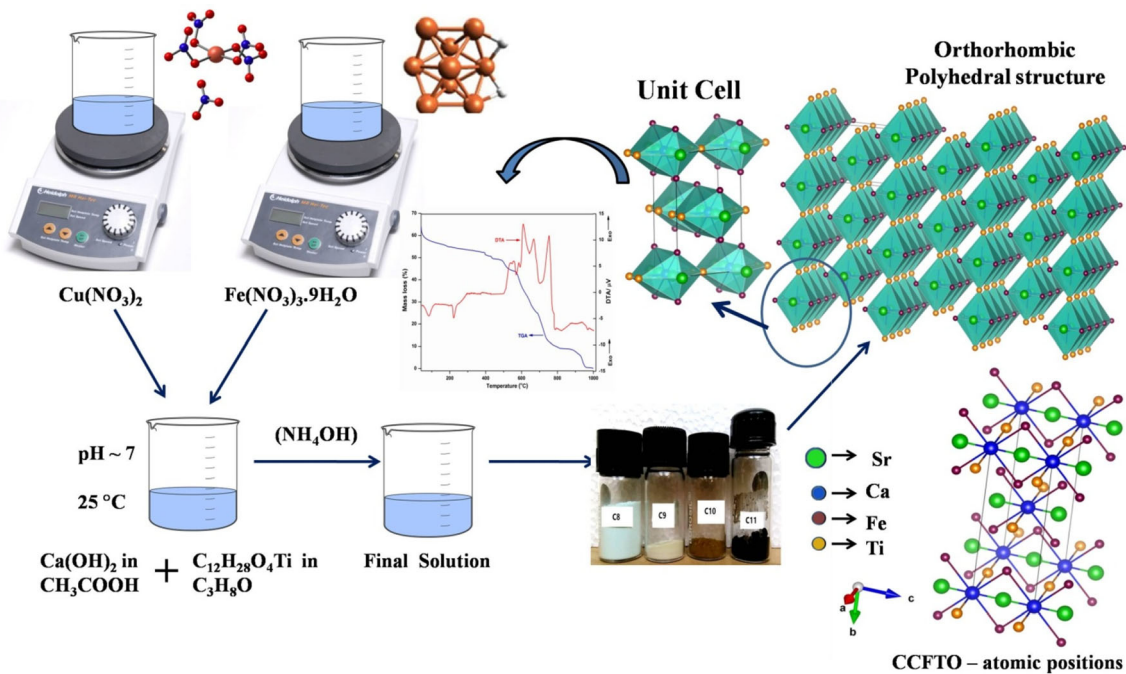
Fig. 1 Protocol of synthesizing Cu:CTF nanoperovskites

higher magnitudes of about 1,000,000 X. Also, the micro-images were recorded with an adoptive magnetic imaging filter (GATAN) (Eindhoven, The Netherlands).

The frequency dependence (1 Hz–1 MHz) of complex plane impedance spectroscopy (CIS; Autolab PGSTAT302N, Metrohm, The Netherlands) was used to examine the electrical properties such as capacitance (F), resistance (Ω), phase data (ϕ), dielectric constant (ε′), tangent loss (tan δ), and *ac* conductivity (σac) with respect to grain and grain boundaries. The dc conductivity of the samples was studied with respect to inverse temperature (1/T) using LCR Hi-Tester (HIOKI, Model No: 3532–50, Japan) ranging from ambient temperature to 250 °C with 100 µV resolutions. Impedance and electrical properties for pelletized CCFTO specimen was obtained from Autolab instrument using Swagelok-type cell setup [28].

3 Results and discussion

The physical changes that Cu:CTF undergo during the rise in temperature was analyzed using TG/DTA analysis. Figure 2 shows the TG/DTA measurements of Cu:CTF powder pre-heated at 100 °C for 24 h. From the Fig. 2, it is evident that pure crystal nature

appears above 750 °C. The theoretically calculated density for all the electroceramic samples sintered in air was 5239 kg m^{-3}, 5315 kg m^{-3}, 5627 kg m^{-3} and 5388 kg m^{-3} respectively for C8, C9, C10 and C11. The grain growth in Cu:CTF perovskite materials get intensified with increase in temperature which is apparently evident from the SEM micrographs as shown in Fig. 3.

This may be due to the development of pores in the sample during the sintering process leading to the increased density of 95%. It was also observed that beyond certain temperature ($\sim$ 1000 °C), the density gets decreased [10, 26]. In addition, the density of sample C11 is found smaller compared to other samples because after reaching 1100 °C, Cu:CTF nanotitanate loses its stability and starts to form loosened agglomerated structures. This is due to mass increases with decrease in volume expansion and drastic increase in pressure for the samples sintered at above 1000 °C [26]. The Cu:CTF material shows optimum performance till $\sim$ 1000 °C, and can be used at higher temperatures below the threshold point (1000°C) for efficient SOFC electrodes.

Figure 3 depicts the X-ray diffraction graph of Cu-doped Ca(Ti$_{0.9}$Fe$_{0.1}$)O$_{3-\delta}$ perovskite samples sintered at different temperatures (800–1100 °C). The existence of orthorhombically tilted perovskite structure

Fig. 2 Thermogravimetry and differential thermal analysis (TG/DTA) of Cu:CTF as-prepared powder pre-heated at 100 °C for 24 h
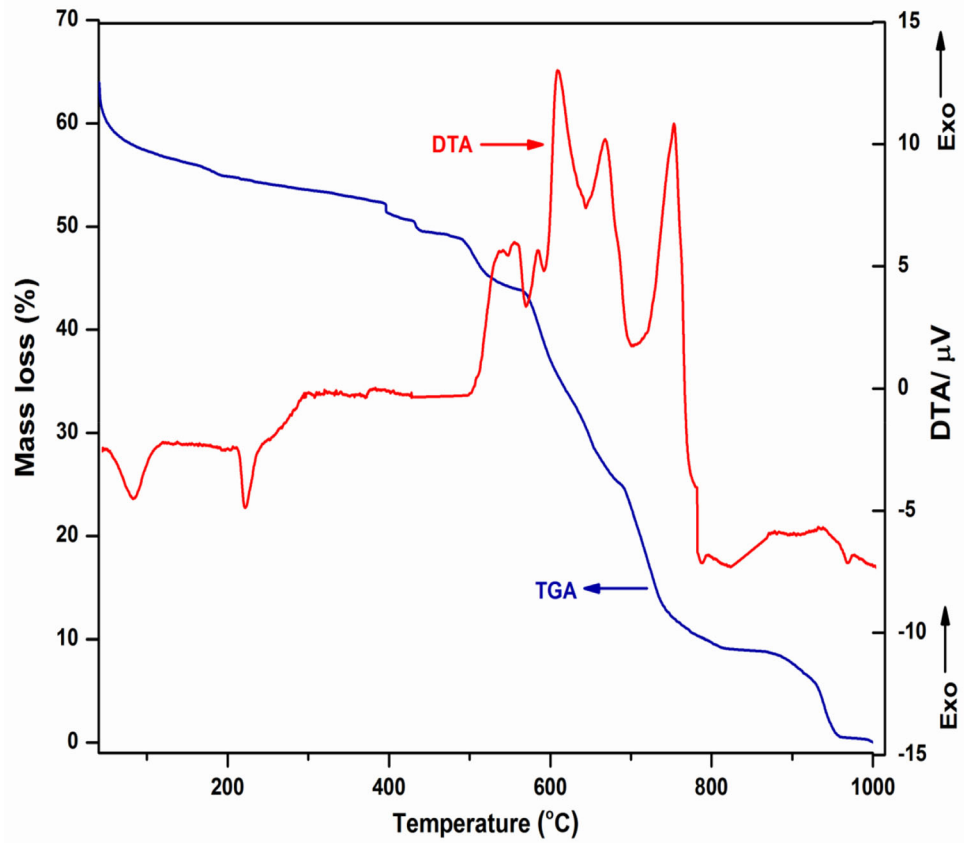
is observed for all the sintered Cu:CTF nanotitanates. The diffraction positions for the sintered perovskite samples were in good agreement with orthorhombic phases of $CaTiO_3$ (JCPDS card No. 72–1192) indexed with space group, *Pcmn*. Further, the XRD pattern showed some secondary phases with small traces of $CaCu_2O_3$ (CCO), TiO_2, CuO [29, 30]. Moreover, TiO_2 and CuO get vanished when sintering condition reaches higher order ($\geq$ 900 °C).

Additionally, the minor peaks were observed between 25° and 32° in Cu-doping $Ca(Ti_{0.9}Fe_{0.1})O_{3-\delta}$ perovskite, which are identified as $CaTiO_3$ trace phase. It is clear that the first three strong peaks of sintered polycrystalline powders namely, (101) at 23.24°, (121) at 33.08° and (202) at 47.54° matched with the standard perovskite orthorhombic structure [31]. Further, increase in temperature results in strong peaks at 2θ = 35.2°, 36.4° and 37.9°, respectively for (111), (400) and (301) planes attributed to CCO emerging from orthorhombic (JCPDS card No. 71–2295) phase for C9-C11 samples with a space group of *Pmmn*, while C8 sample exhibit weak diffraction peaks in this criterion.

Therefore, the present crystal is still in the orthorhombic phase structure owing to TiO_6 octahedral long-range tilting, thus, enhancing oxygen vacancies for transportation properties [32, 33]. As the temperature of the crystalline Cu:CTF increases, the spacing distance between the Fe and Cu ion increases in the crystal lattice. In contrast, useful double-peak features from temperature phenomena indicate that solid–solid phase transitions can be broadly known for Cu:CTF perovskite [32–35]. However, the phenomena indicate an increase in the temperature of the crystal size without modifying the crystal type. An increase in temperature increases the grain size, but reduces the density of the Cu:CTF nanoperovskite material [12]. The average crystallite size of Cu:CTF materials is estimated by Scherrer's formula (Eq. 2) which is in range of 51–72 nm. The lattice parameter data and the average crystal size are listed in Table 1.

Typical SEM image of prepared Cu-doped CTFO perovskites at different sintering temperatures are shown in Fig. 4a–d. It is clearly evident that micro-grains of the sintered Cu:CTF powders are highly

Fig. 3 Powder XRD pattern for all sintered Cu:CTF perovskite nanotitanate samples sintered at different temperatures
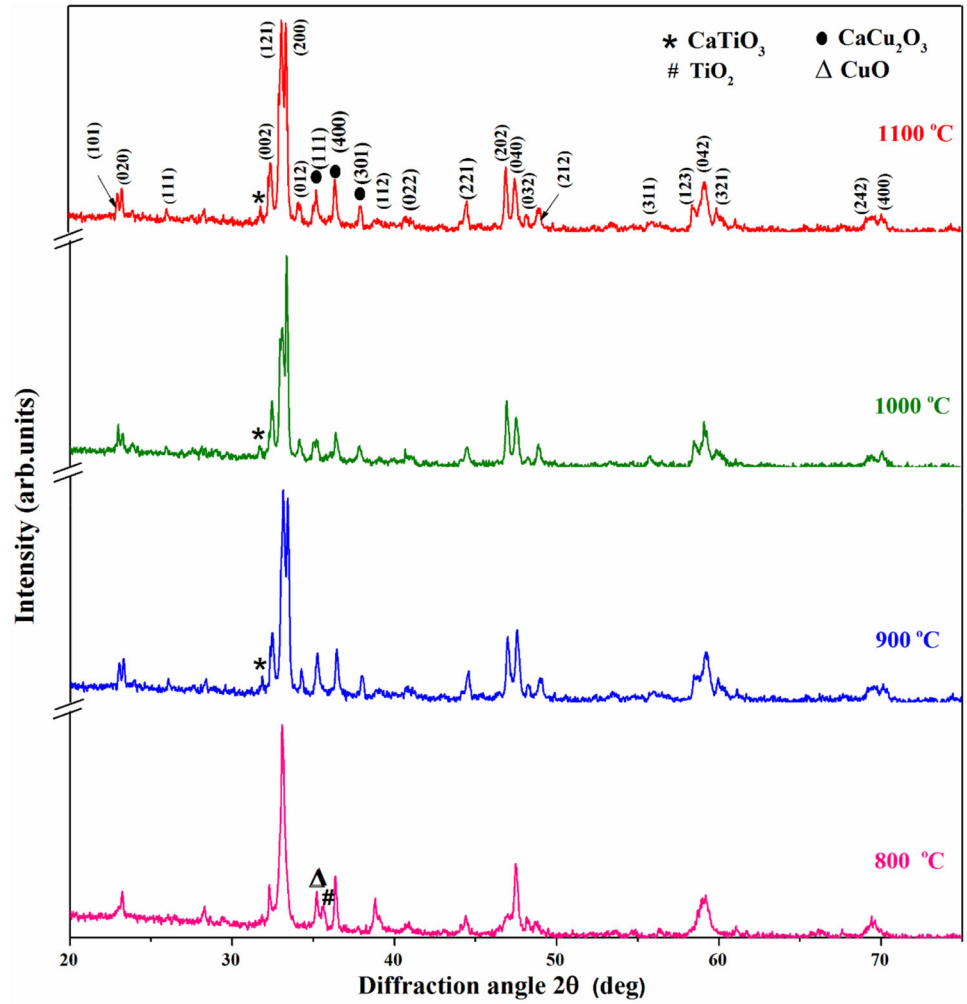

Table 1 Lattice parameters and average crystal size for Cu:CTF nanotitanates at different temperatures

Sintering temperature (°C)	Sample code	Lattice parameters					Average crystal size (nm)	Tolerance factor (t_f)
		a (Å)	b (Å)	c (Å)	c/b	V_{cell} (Å)^3		
800	C8	5.3803	7.6352	5.4407	0.7125	223.50	51.22	0.7673
900	C9	5.3824	7.6396	5.4435	0.7125	223.83	58.58	0.7685
1000	C10	5.3851	7.6387	5.4421	0.7124	223.86	61.69	0.7689
1100	C11	5.3879	7.6463	5.4468	0.7123	223.39	72.36	0.7706

dense and strongly agglomerated at temperature below 900 °C. Meanwhile, the particles are strongly agglomerated leading to an increase in densification and an increase in the size of grains with an increase in sintering temperature (800–1100 °C) [33]. When sintering temperature reaches 1100 °C, the powder gets loosen state and hence, the density of the C9

sample decreases. It is clear that the average grain size of the sintered powder obtained from SEM micrographs is in the range of 66–217 nm.

Crystallite size of Cu:CTF materials is far different from the size estimated from SEM. It reported that XRD crystallite size, however the particle size observed from SEM looks like a particle is
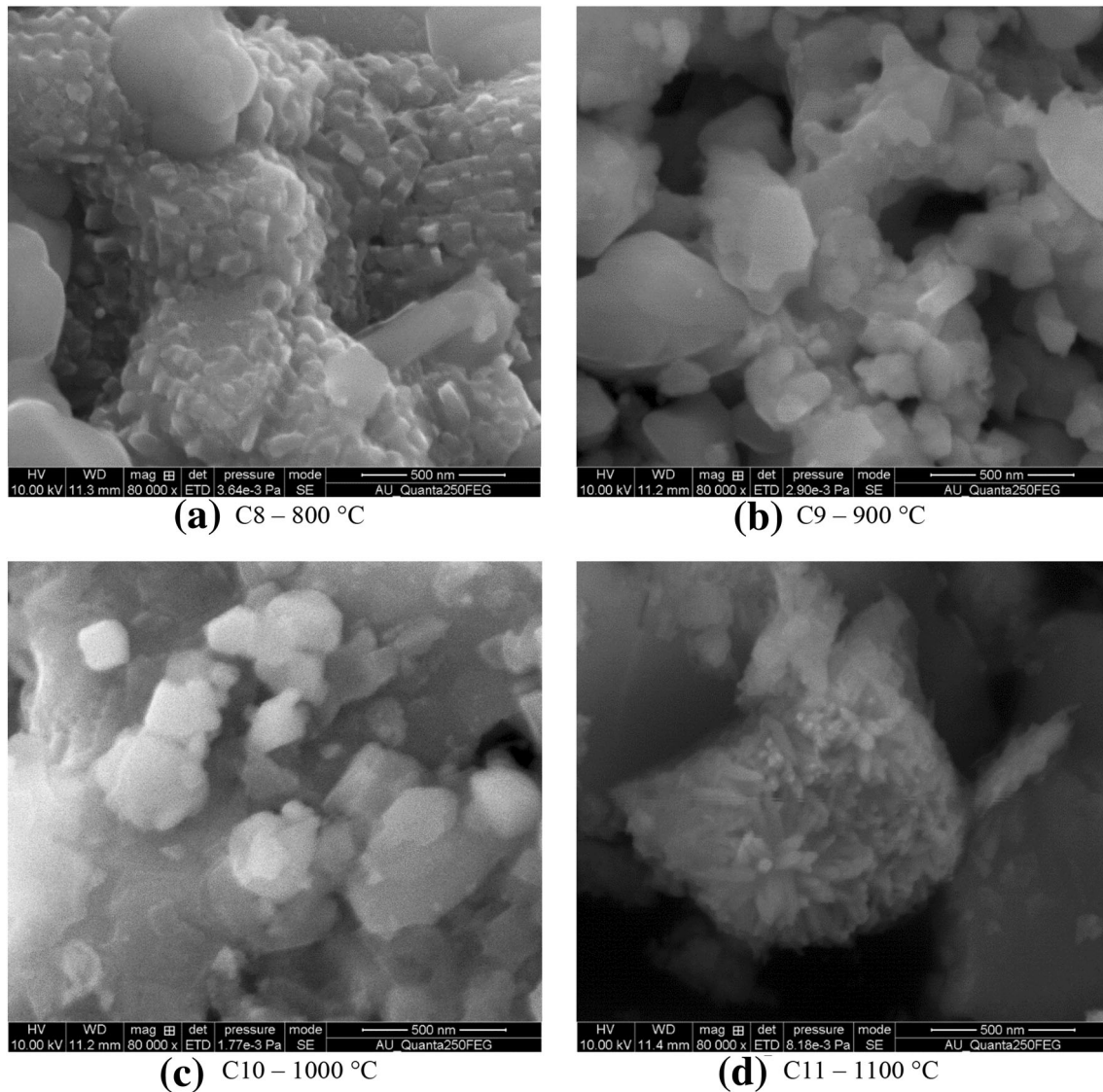
Fig. 4 SEM images of Cu:CTF nanotitanates treated at (**a**) 800 °C, (**b**) 900 °C, (**c**) 1000 °C, and (**d**) 1100 °C for 8 h

combination of several crystallites and revealed with faceted forms [36, 37]. Figure 5 show the typical bright-field TEM image of Cu-doped CTF powders sintered at 900 °C. Particle sizes of the prepared CSTF lies between 52 and 190 nm. The inset (SAED pattern) associated with TEM depicts Cu:CTF nanoperovskite are symmetrical and highly crystalline as shown in Fig. 5 [38]. As a result of better crystallization under high temperature, the geometric theory of grains becomes more complex due to the uniformity with higher temperatures [39]. Therefore, high temperature causes the larger grain growth, resulting in sharp edged crystals [40, 41].

The room temperature UV–visible absorption spectra of all the Cu doped CTF samples sintered at different temperatures are shown in Fig. 6(a). It is found that the existence of absorption spectra of the sintered nanotitanates is exhibited in the range from 228 to 234 nm. Therefore, the addition of sintering temperature further reduces the intensity of absorption peaks and hence, convolutes dominance of Cu:CTF nanotitanate perovskite material in the visible region. The absorbance wavelength of a material plays a vital role in estimating the electron transitions, charge carrier concentration, conductivity and electrode activation energies etc. The optical properties (direct and indirect band gap) of Tauc relation through spectral line intercept for the prepared Cu:CTF crystalline perovskites are shown in Fig. 6b and c.
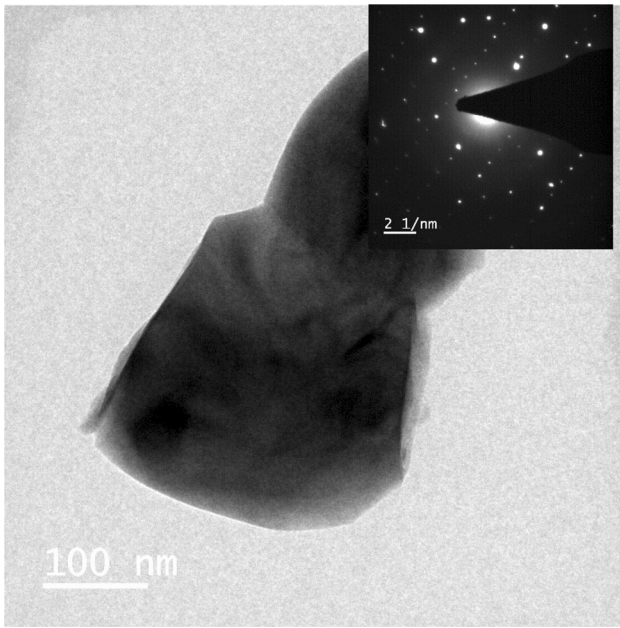
Fig. 5 Typical TEM image for sample C9 with inset SAED pattern

indirect bandgap (IBG) values. The DBG and IBG values are examined using Tauc relation [42],

$$\alpha h\upsilon = A(h\upsilon - E_g)^n \qquad (4)$$

where α the absorption coefficient, A the proportionality constant and n the electronic transition values 1/2 and 2 for allowed direct and allowed indirect transitions, respectively.

The optical parameters associated with UV-absorbance are given in Table 2. It is inferred from the values of band gap energy (E_g) of Cu:CTF nanotitanates, the band gap is increased with increase in the sintering temperature. Hence, the increase in band gap with increase in sintering temperature may be associated with the formation of defects such as oxygen vacancies, microstrain etc. [43]. As can be seen from the direct and indirect band transition calculations, indirect band gap values are deviated from one which determined from Max Planck's energy equation (Eq. 3). Therefore, it could be infer-
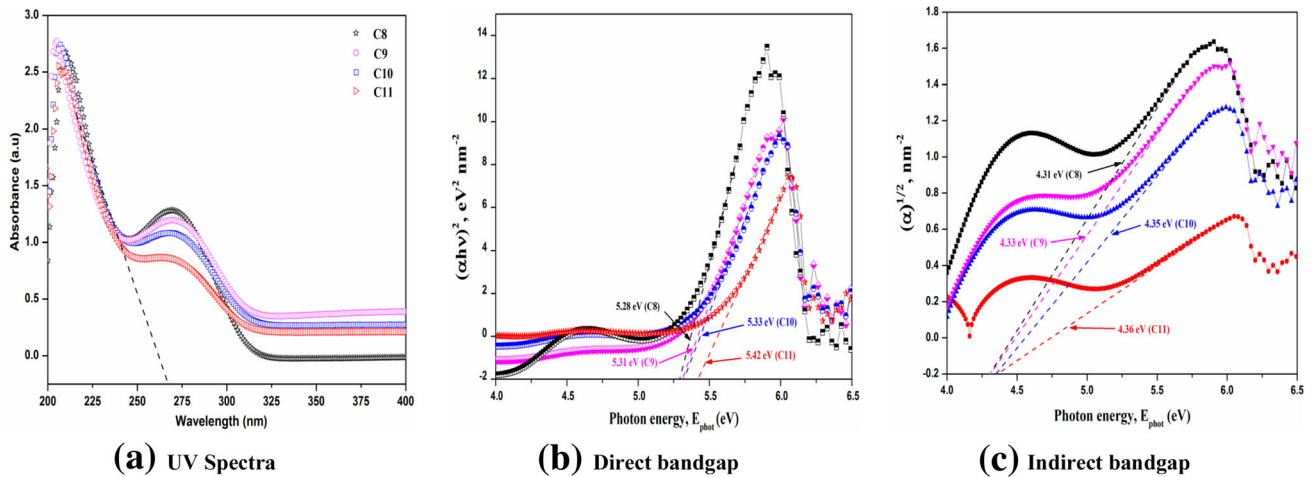

(a) UV Spectra   **(b)** Direct bandgap   **(c)** Indirect bandgap

Fig. 6 **a** UV–vis absorption spectra, **b** Direct band gap and, **c** Indirect band gap for all sintered Cu:CTF perovskites at room temperature

The band gap energy (E_g) of the samples were obtained using the following Max Planck's energy equation,

$$E_g = \frac{h\upsilon}{\lambda} \qquad (3)$$

where E_g the band gap energy, $h\upsilon$ is the photon energy in eV, and λ the wavelength of absorption.

UV–vis spectrometer data can be used to calculate the band differences (conduction band and valence band) of mixed metal oxides adopting semiconductor behaviours such as direct bandgap (DBG) and

red that direct band transition values are more relevant with estimated band gap values than indirect transition ones.

Impedance spectroscopy is very effective method to obtain loss and gain features as resistive and reactive components through grain, grain boundary and electrode interface, in a complex system when an a.c. bias is applied. Figure 7 shows the Nyquist plot (Cole–Cole) of impedance spectra as a function of frequency (1 Hz–1 MHz) for prepared Cu:CTF perovskite material sintered at different temperatures. At high sintering temperature, the semicircle arc

Table 2 UV -vis absorbance and bandgap energy values of Cu:CTF nanotitanates

Sample code / Sintering Temperature (°C)	Absorbance (nm)	Max Planck's energy (eV)	Direct Bandgap (eV)	Indirect Bandgap (eV)
C8 / 800	234	5.29	5.28	4.31
C9 / 900	233	5.31	5.31	4.33
C10 / 1000	232	5.34	5.33	4.35
C11 / 1100	228	5.43	5.42	4.36

Fig. 7 Nyquist plot for Cu:CTF samples sintered at different temperatures
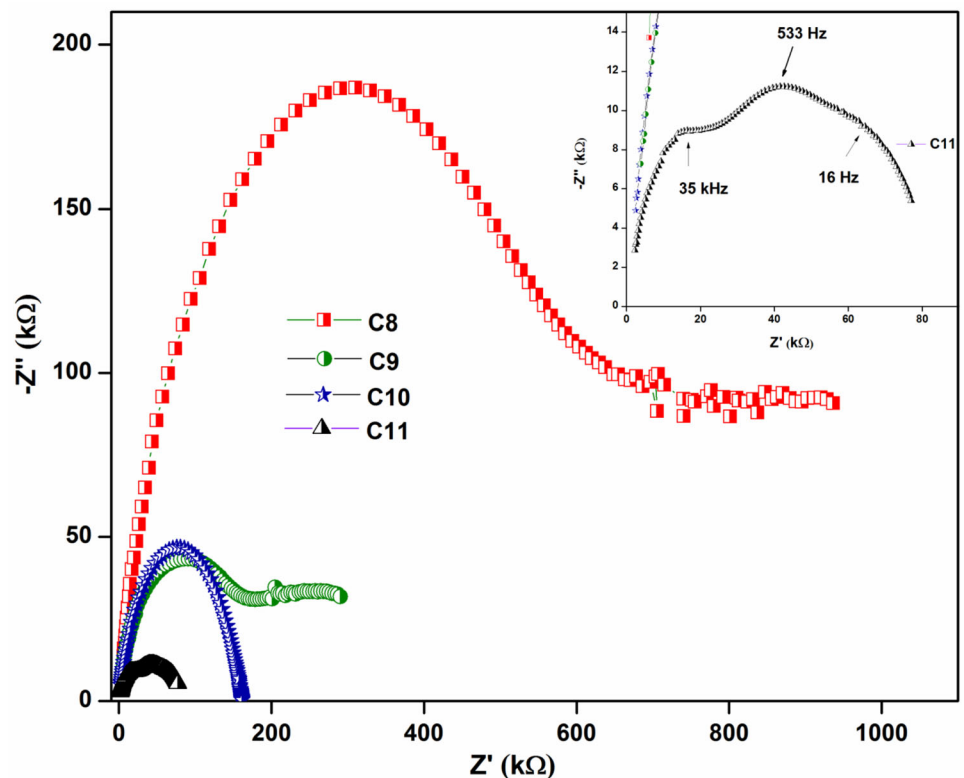
tending to form with larger diameter of sample C8 than that of sample C11 and it decreases when the temperature increases.

At high sintering temperature, a change in the microstructural is observed in the samples and thus reduces the impedance at interface thereby resulting conductivity improvement. As can be seen from the Fig. 7, the semicircles present in all samples with non-zero intercept Z′ and with no semicircle are ascribed to grain boundary and grain-electrode interface, respectively [44] Thus, the decrease in resistance of grains and grain boundaries with rise in temperature shows semiconductive behaviour of the prepared compounds i.e., negative temperature coefficient of resistance (NTCR) effect [45].

The expanded view of Z′ vs Z″ for sample C11 is shown in Fig. 7 that depicts the sake of clarity of two semicircles, a small one and a large one. It can be seen that a small and large semicircle at high and low frequencies indicated the effect of grain and grain boundary contribution of conductivity, respectively. To contribute the total resistances observed for the compound C8-C11, the RC element model associated with grain (R_g; semiconductive) and grain boundary (R_{gb}; insulative barrier) is proposed. The distribution of smaller grains present in the sintered samples is modelled with an ideal equivalent circuit consisting of RC parallel elements of the material. A series resistor (R_1) is added in all the equivalent circuits

corresponding to the high frequency intersection of the origin of the plot.

The values of respective grain (C_g) and grain boundary (C_{gb}) capacitances were determined from the relation $\omega_{max} = 1/RC$, where ω is the maxima angular frequency ($\omega = 2\pi f$, f is frequency in Hz) [46]. From the equivalent circuit, the obtained values of resistance and capacitances attributing to respective grains and grain boundaries are tabulated in Table 3. It is also observed that, especially the co-existence of three RC phase element model obtained from the equivalent circuit for compound C11 is as R_eC_e, where R_e is the medium frequency resistance and C_e is the electrode contact capacitance.

Figure 8 shows the Bode phase plot of impedance spectra for Cu-doped CTF at different temperatures. The characteristics plot between frequency vs phase angle and |Z| simultaneously exhibits a tendency of forming the linear decrement in their both values. It is notably, the variation of phase angle decreases when the sintering temperature increases (Table 3).

The room temperature measurement for the frequency dependence of the dielectric properties of the crystalline Cu-doped CTFO nanotitanates is shown in

Fig. 9a and b. It can be seen from the Fig. 9a, the value of dielectric constant (ε') increases with increase of temperature, while decreases with increase in frequency for all sintered samples. Thus, the phenomena reveal that the ε' obeys both relaxation and deformational polarization facts [47]. Notably, a giant dielectric constant value up to $\sim 10^5$ in the low frequency range is denoted as Maxwell–Wagner polarisation at room temperature. This indicates Cu:CTF material treated at 1100 °C is monotonically decreased to $\varepsilon' \sim 40$ in the MHz range. Similarly, the variation of dissipation factor (tan δ) is also declined gradually towards higher frequency with very low loss tangent values as shown in Fig. 9b [48]. The dielectric and loss tangent values corresponding to selectable frequency is depicted in Table 4.

Figure 10a–d shows the combined plots of imaginary part of electric modulus and impedance loss spectra as a function of frequency for Cu:CTF with different sintering temperatures. It is observed that Z'' and M'' both have single peaks are found to be clear for all sintered compounds. The maximum of the peaks shift towards higher frequency on

Table 3 Impedance parameters and activation energy (E_a) values of Cu:CTF nanotitanates at different sintering temperatures (S)

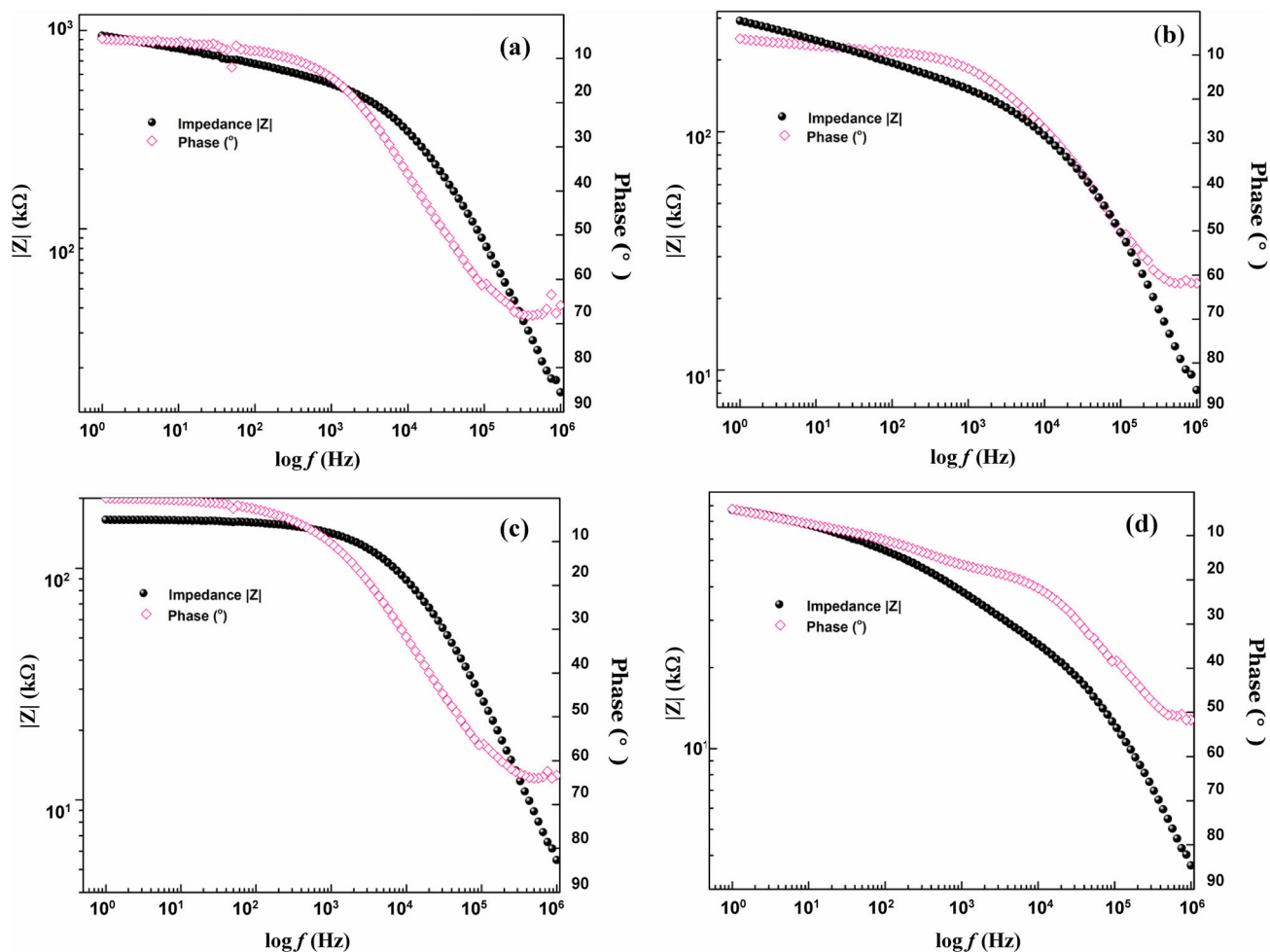| S (°C)	Bode angle (°)	R_g (kΩ)	C_g (F)	R_{gb} (kΩ)	C_{gb} (nF)	R_e (kΩ)	C_e (nF)	σ_{ac} (Ω^{-1} cm^{-1})	E_a (eV)	Equivalent electric circuit
800	65.9	607.8	3.98×10^{-11}	1094.2	0.414	–	–	1.98×10^{-4}	0.58	
900	61.8	178.5	1.24×10^{-10}	359.4	0.856	–	–	3.81×10^{-4}	0.46	
1000	63.3	161.2	1.13×10^{-10}	128.6	1.582	–	–	8.51×10^{-4}	0.47	
1100	51.6	34.4	1.50×10^{-10}	62.4	4.865	79.1	0.014	1.71×10^{-3}	0.37	

Fig. 8 Bode plots of Cu:CTF nanotitanates sintered at **a** 800 °C, **b** 900 °C, **c** 1000 °C, and, **d** 1100 °C

increasing temperature followed by strong frequency dispersion phenomena occurs for Z'' and M''. The distribution of relaxation time (τ) behaviour is analysed for each sample with respect to peak width, which is being broadened when temperature elevates. However, the M''_{max} with respect to low frequency region responsible for the charge carriers are active on long distances, while the higher frequency region is responsible for the charge carriers are active on short distances [49].

In this relaxation mechanism, oxygen ions exhibit diffusivity between Fe^{3+}-O-Fe^{2+} and Ti^{4+}-O-Ti^{3+} in such a way that the delocalized relaxation takes place. Hence, it is clearly shows that the Z'' and M'' peaks observed for all the samples are compressed and shifted to high frequency region with rise in sintering temperature. The relaxation behaviour from the obtained plots reveals all the samples sintered above 800 °C attained hopping mechanism of

electrical conduction in the perovskite materials due to temperature-dependent dielectric relaxation. In addition, the correlation between mobility of charge carriers in terms of dielectric relaxation is thermally activated process [10].

Figure 11 shows the frequency dependence of a.c. conductivity (σ_{ac}) for different sintered Cu-doped $CaTi_{0.9}Fe_{0.1}O_{3-\delta}$ nanotitanates measured at room temperature. It reveals that the values of σ_{ac} for all the samples increase with increasing sintering temperature. In addition, the dispersion-related conductivity as a function of frequency may be attributed to the fact as follows, (i) The interface polarization effects are response for d.c. conduction, where the dipoles are trapped by low frequency i.e., frequency-independent conductivity, (ii) The long-range displacement of ionic dipoles tending to become active at middle region frequencies, and (iii) Finally, the oxygen defect processes leads to increasing of
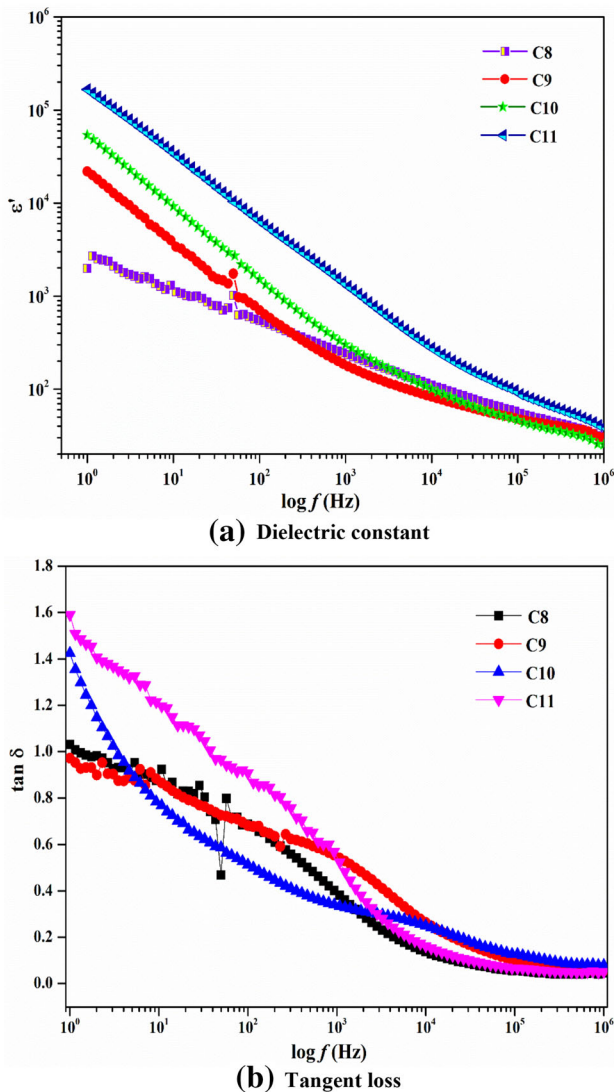
(a) Dielectric constant

(b) Tangent loss

Fig. 9 Frequency dependence of (**a**) real part permittivity and (**b**) tangent loss at room temperature for Cu:CTF perovskite

conduction due to localized mobile ions with increase of frequency [10].

Nevertheless, the sintering temperature also an important factor which in turns hopping of polarons (ω_P) with increase in frequency. Therefore, the interpretation of high-frequency dispersion phenomenon for Cu:CTF not only depends on frequency but also its charge carriers are apparently agitated by thermally activated process. This phenomenon of the conductivity dispersion in solids is strongly exhibited by small polaron hopping. At low frequency, the phenomenon of the conductivity dispersion in solids strongly exhibits small polaron hopping, which was normally analysed using the relation of Jonscher's power law [50, 51],

$$\sigma_{ac} = \sigma_{dc} + A\omega^s = \sigma_{dc}[1 + (\omega/\omega_p)^s] \tag{5}$$

where σ_{ac} is the ac frequency component, σ_{dc} is the dc conductivity at certain temperature, A is the intrinsic property of a material constant, ω is the angular frequency, ω_p is the frequency of hopping and s is the dimensionless quantity ranging between 0 and 1, which is a strong temperature dependent property of the material [10, 25, 51].

The dc conductivity studies were done under the experimental temperature ranges from 27 to 250 °C for the prepared Cu:CTF samples are shown in Fig. 12. It can be seen that the d.c. normalized curves for all the samples decreases with increase in temperature (resistivity decreases) and hence the material exhibits NTCR effect [47]. Hence, the prepared nanotitanates possess *Arrhenius type* of conductivity along with thermally agitated transport mechanism,
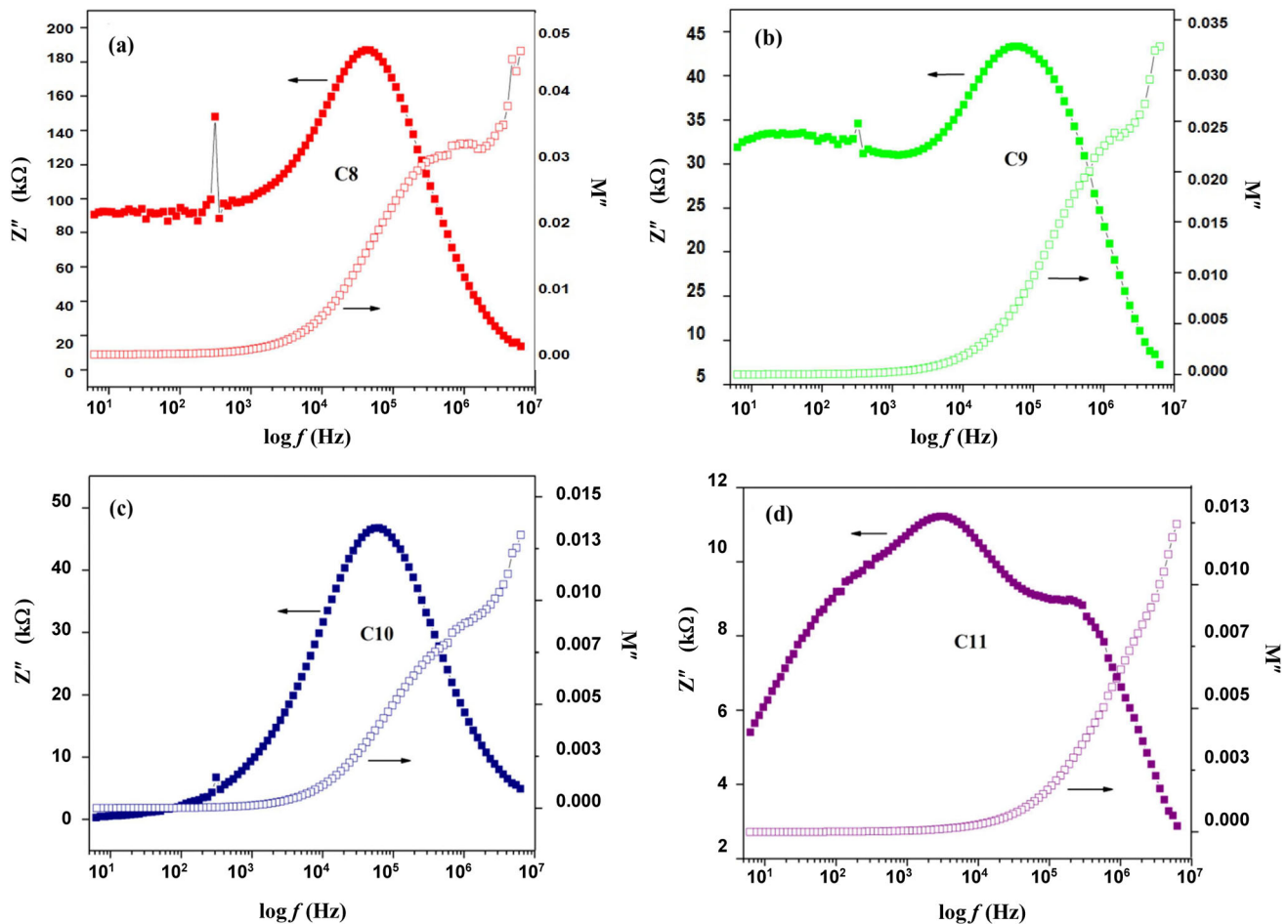
Table 4 Dielectric constant and loss tangent values for Cu:CTF samples at selected frequencies

Frequency (Hz)	Samples							
	C8		C9		C10		C11	
	ε'	tan δ	ε'	tan δ	ε'	tan δ	ε'	tan δ
10	1314	0.864	1768.32	0.923	6809.03	1.226	34,721.21	1.497
1×10^3	233.61	0.641	61.88	0.658	180.22	0.864	1283.26	0.472
10×10^3	110.76	0.503	24.91	0.336	55.90	0.529	277.35	0.416
100×10^3	54.85	0.235	13.46	0.115	24.50	0.216	88.37	0.134
1000×10^3	30.47	0.073	7.96	0.044	12.83	0.098	39.06	0.050

Fig. 10 The variation of Z″ and M″ as a function of frequency for Cu:CTF nanotitanates at different temperatures

and the conduction can be expressed by the following relation [10, 52],

$$\sigma_{dc} = \sigma_o \exp\left[\frac{-E_a}{K_B T}\right] \qquad (6)$$

Where σ_o is the pre-exponential term, E_a is the activation energy, and k_B denotes Boltzmann constant. The fitting lines of dc conductivity were plotted through $ln\sigma_{dc}$ Vs inverse of temperature (1/T) and its corresponding activation energies for different sintered compounds are found in Table 3. The calculated activation energies from the above relation (Eq. 6) were in the range between 0.58 and 0.37 eV due to oxygen defects. The formation of anionic vacancies in Cu:CTF nanotitanate proves the mixed ionic and electronic conductivities of oxygen, by exhibiting oxygen vacancies as structural defect and increased electronic conductivity, which makes the material optimum for fuel-cell electrodes and electrocatalysts.

4 Conclusion

In this present work, we synthesized and report the Cu-doped $Ca(Ti_{0.9}Fe_{0.1})O_{3-\delta}$ (CTF) nanotitanates was prepared by sol–gel technique and heat treated at various temperatures (800 – 1100 °C). The crystalline phase formation of the nano-crystalline Cu:CTF was examined around ≥ 750 °C employing TG/DTA analysis. The room temperature XRD analysis confirms the formation of poly-phase ceramics with orthorhombic structure. Another orthorhombic structure with different symmetry group was identified above 800 °C. It was found that the measured density of the sample C10 was significantly higher than the other samples. The SEM image of sintered Cu:CTF ceramic shows particles with uniform distribution at 800 °C, whereas C9-C11 reveals random and inhomogeneous grains distribution as temperature elevates. The particle sizes were measured from TEM image and were in the range of 52–190 nm. The

Fig. 11 Variation of ac conductivity (σ_{ac}) as a function of frequency of Cu:CTF nanotitanates
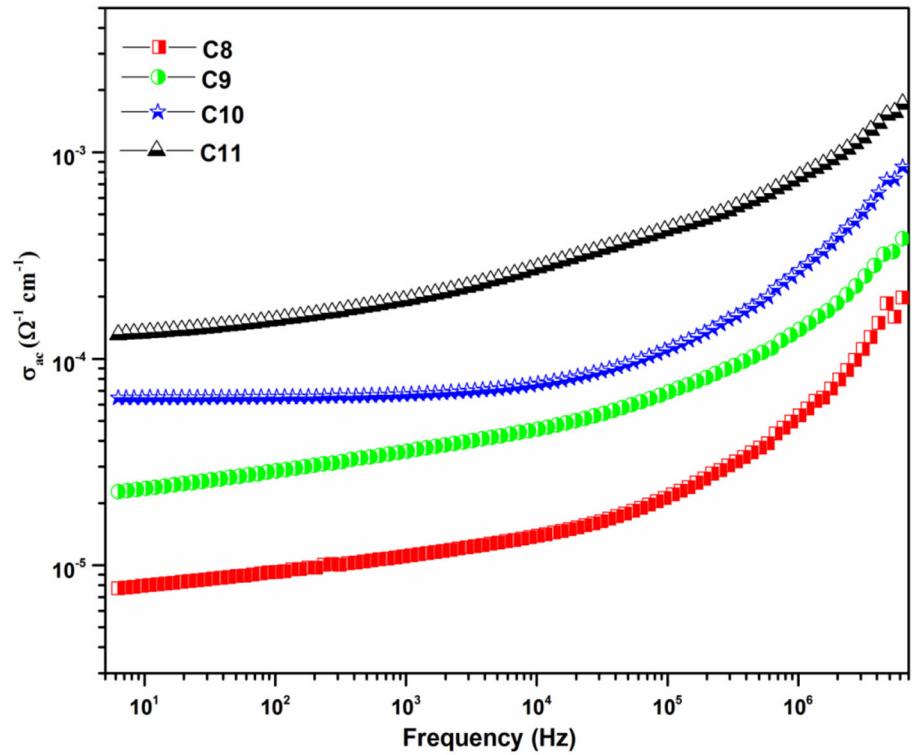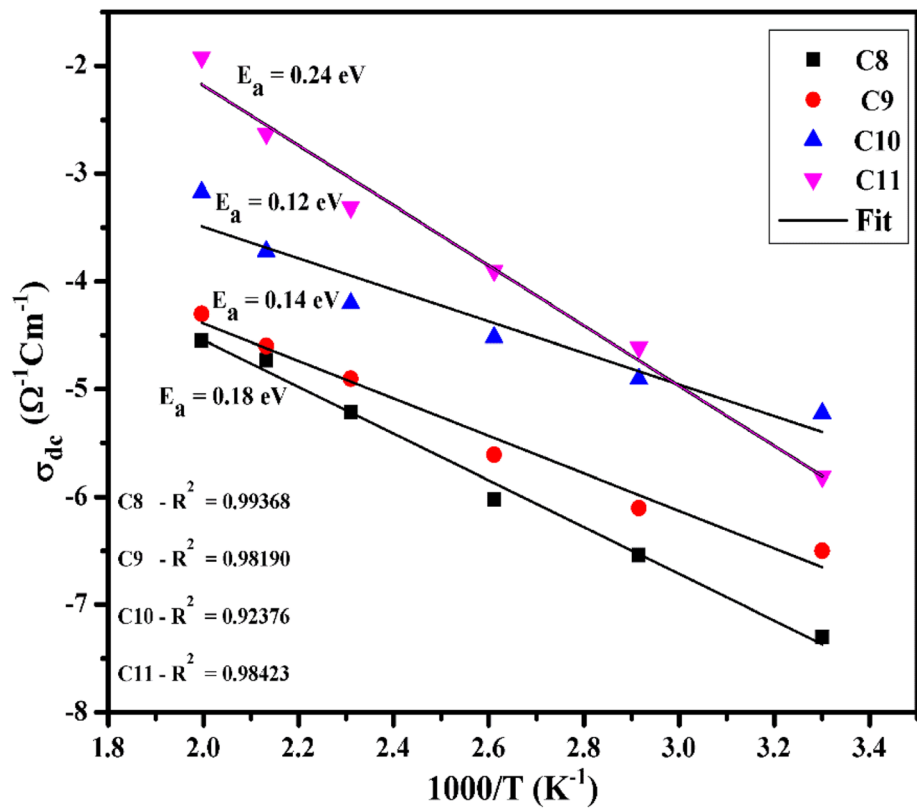

Fig. 12 Variation of dc conductivity (σ_{dc}) as a function of inverse of absolute temperature for Cu:CTF nanotitanates

optical band gap energy calculated from the UV-Vis absorbance spectral lines shows that all the prepared

nanotitanates possess insulative behaviour close to red shift region with the band gap variation of

5.28–5.42 eV. Electric modulus spectrum shows that the relaxation variation with different time constant, confirming Cu:CTF is a non-Debye type material. The increase in frequency with respect to increase in ac conductivity may be ascribed to mobility carrier hopping mechanism at shorter ranges. Sample sintered at 900 °C exhibited higher dielectric constant (1.7×10^3) with moderate tangent loss (0.926) when compared to other samples. As a result of the larger grain size, the overall conductivity obtained for Cu:CTF nanotitanate samples are improved. The eminent versatility of this perovskite structure allows different doping to obtain a variety of properties, which is a spot-light in the development of solid oxide fuel cell (SOFC) electrode materials. Thus, the improved dielectric properties and NTCR effect was concern, the Cu-doped $Ca(Ti_{0.9}Fe_{0.1})O_{3-\delta}$ nanotitanates can act as supportive electrode catalysts for SOFCs.

Availability of data and material

Data will be available on request.

Code availability

Not applicable

Declarations

Conflicts of interest The authors declare that they have no conflict of interest.

Ethical approval Hereby, we declare that the manuscript is our original work and not have been published or under editorial considerations anywhere else. The stated authors of the work, have read the content and approved for submission of this manuscript to Journal of Materials Science: Materials in Electronics. There is no personal or financial conflict of interest. Further if our article has been accepted, we ensure that we will not publish it anywhere else in any form, in any language without getting consent of the publisher.

References

1. K. Kendall, High-Temperature Solid Oxide Fuel Cells for the 21st Century Portable early market SOFCs, 2nd edn, (Academic Press, Boston), **10,** 329–356 (2016).
2. K. Kendall, Introduction to SOFCs, in: K. Kendall, M. Kendall High-Temperature Solid Oxide Fuel Cells for the 21st Century, 2nd edn, (Academic Press, Boston), **1,** 1–24 (2016).
3. K. Kendall, High-Temperature Solid Oxide Fuel Cells for the 21st Century, 2nd edn, (Academic Press, Boston), **2,** 25–50 (2016).
4. A.B. Stambouli, E. Traversa, Solid oxide fuel cells (SOFCs): a review of an environmentally clean and efficient source of energy. Renew. Sust. Energ. Rev **6**, 433–455 (2002)
5. N.P.B. Mihails Kusnezoff, Andrew Gyekenyesi, Michael Halbig, Advances in Solid Oxide Fuel Cells X, International Symposium on Solid Oxide Fuel Cells: Materials, Science, and Technology, John Wiley and Sons, Florida, 144 (2014).
6. A. Atkinson, S. Barnett, R.J. Gorte, J.T.S. Irvine, A.J. McEvoy, M. Mogensen, S.C. Singhal, J. Vohs, Advanced anodes for high-temperature fuel cells. Materials for Sustainable Energy, Co-Published with Macmillan Publishers Ltd, UK **1**, 213–223 (2010)
7. N. Mahato, A. Banerjee, A. Gupta, S. Omar, K. Balani, Progress in material selection for solid oxide fuel cell technology: A review. Prog. Mater. Sci. **72**, 141–337 (2015)
8. M.A. Ramírez, P.R. Bueno, J.A. Varela, E. Longo, Non-Ohmic and dielectric properties of a Ca2Cu2Ti4O12 polycrystalline system. Appl. Phys. Lett. **89**, 212102 (2006)
9. T.-T. Fang, H.-K. Shiau, Mechanism for developing the boundary barrier layers of $CaCu_3Ti_4O_{12}$. J. Am. Ceram. Soc **87**, 2072–2079 (2004)
10. X. Song, Y. Zhang, Y. Chen, Z. Shen, T. Zhang, Effect of sintering atmosphere on the microstructure and dielectric properties of barium strontium titanate glass–ceramics. J. Mater. Sci.: Mater. Electron. **29**, 56–62 (2018)
11. B. Kamecki, T. Miruszewski, J. Karczewski, Structural and electrical transport properties of Pr-doped $SrTi_{0.93}Co_{0.07}O_{3-\delta}$ a novel SOEC fuel electrode materials. J. Electroceram. **42**, 31–40 (2019)
12. M.A. Ahmed, S.T. Bishay, Effect of annealing time, weight pressure and Fe doping on the electrical and magnetic

behavior of calcium titanate. Mater. Chem. Phys. **114**, 446–450 (2009)

13. R.K. Pandey, W.A. Stapleton, J. Tate, A.K. Bandyopadhyay, I. Sutanto, S. Sprissler, S. Lin, Applications of CCTO supercapacitor in energy storage and electronics. AIP Adv. **3**, 062126 (2013)

14. M. Gazda, P. Jasinski, B. Kusz, B. Bochentyn, K. Gdula-Kasica, T. Lendze, W. Lewandowska-Iwaniak, A. Mielewczyk-Gryn, S. Molin, Perovskites in solid oxide fuel cells, in solid state phenomena. Trans Tech Publications Ltd. **183**, 65–70 (2012)

15. E.D. Wachsman, K.T. Lee, Lowering the temperature of solid oxide fuel cells. Science **334**, 935 (2011)

16. Panday, M. Sridhar, M. Vinoth, S. Surendhiran, V. Rajendran, and P. Susthitha Menon, Investigation on electrical conductivity of strontium (Sr^{2+}) influenced $CaTi_{0.8}Fe_{0.2}O_3$ polycrystalline perovskite, In 2016 IEEE International Conference on Semiconductor Electronics (ICSE), 192–195. IEEE, 2016.

17. S.-Y. Chung, S.-Y. Choi, T. Yamamoto, Y. Ikuhara, Inherent nanoscale bend of crystal lattice in Fe-doped calcium copper titanate. Appl. Phys. Lett. **89**, 121903 (2006)

18. J. Wang, L. Feng, A. Lei, K. Zhao, A. Yan, Preparation and dielectric properties of $CaCu_3Ti_4O_{12}$ ceramics with different additives. J. Mater. Eng. Perform. **23**, 3133–3140 (2014)

19. N. Raeis Hosseini, N.M. Sammes, J.S. Chung, Manganese-doped lanthanum calcium titanate as an interconnect for flat-tubular solid oxide fuel cells, J. Power Sources **245**, 599- 608 (2014).

20. A. Bandyopadhyay, S. Mondal, M. Pal, U. Pal, M. Pal, Effect of Iron substitution on structure and optical properties of nanocrystalline $CaTiO_3$. J. Nano Res **3**, 123–128 (2008)

21. P.H.B.J.S. Jang, J.S. Lee, K.T. Lim, O.S. Jung, E.D. Jeong, J.S. Bae, H.G. Kim, Photocatalytic hydrogen production in water-methanol mixture over iron-doped $CaTiO_3$. Bull. Korean Chem. Soc. **32**, 95–99 (2011)

22. L. Zhao, K. Chen, Y. Liu, B. He, A novel layered perovskite as symmetric electrode for direct hydrocarbon solid oxide fuel cells. J. Power Sources **342**, 313–319 (2017)

23. F.M. Figueiredo, M.R. Soares, V.V. Kharton, E.N. Naumovich, J.C. Waerenborgh, J.R. Frade, Properties of $CaTi_{1-x}Fe_xO_{3-\delta}$ ceramic membranes. J. Electroceram. **13**, 627–636 (2004)

24. H.P. Beck, W. Eiser, R. Haberkorn, Pitfalls in the synthesis of nanoscaled perovskite type compounds. Part I: Influence of different sol–gel preparation methods and characterization of nanoscaled $BaTiO3$. J. Eur. Ceram. Soc. **21**, 687–693 (2001)

25. S.P. Mathu, P.D. Nehru, V. Murugan, K. Arumugam, A. Sundaramoorthy, R. Venkatachalam, Effect of temperature on the electrical properties of nanocrystalline $CaTi_{1-x}Fe_xO_{3-\Delta}$ perovskite. J Mater Sci: Mater Electron. **27**, 620–630 (2016)

26. M.R. Shah, A.K.M.A. Hossain, Structural, Dielectric and Complex Impedance Spectroscopy Studies of Lead Free $Ca_{0.5+x}Nd_{0.5-x}(Ti_{0.5}Fe_{0.5})O_3$, J. Mater. Sci. Technol. **29**, 323–329 (2013).

27. A.L. Patterson, The Scherrer formula for X-ray particle size determination. Phys. Rev. **56**, 978 (1939)

28. S. R. Srither, A. Karthik, M. Selvam, K. Saminathan, V. Rajendran, Karan VIS Kaler. Nano-sized MnO_2 particles produced by spray pyrolysis for a Zn/MnO_2 primary cell: comparative discharge performance studies with their bulk counterparts.“ RSC adv. **4**, 42129–42136 (2014).

29. R. Kumar, M. Zulfequar, L. Sharma, V.N. Singh, T.D. Senguttuvan, Growth of nanocrystalline $CaCu_3Ti_4O_{12}$ ceramic by the microwave flash combustion method: structural and impedance spectroscopic studies. Cryst. Growth Des. **15**, 1374–1379 (2015)

30. M.H. El-Sadek, O.A. Fouad, M.B. Morsi, K. El-Barawy, Controlling conditions of fluidized bed chlorination of upgraded titania slag. Trans. Indian Inst. Met. **72**, 423–427 (2019)

31. D. Astruc, *Nanoparticles and Catalysis* (John Wiley & Sons, USA, 2008)

32. B. Cheng, Y.-H. Lin, H. Yang, J. Lan, C.-W. Nan, X. Xiao, J. He, High Dielectric Permittivity Behavior in Cu-Doped $CaTiO3$. J. Am. Ceram. Soc. **92**, 2776–2779 (2009)

33. J.P. Singh, S. Gautam, P. Kumar, A. Tripathi, J.-M. Chen, K.H. Chae, K. Asokan, Correlation between the dielectric properties and local electronic structure of copper doped calcium titanate. J. Alloys Compd. **572**, 84–89 (2013)

34. B.M. Patil, R.S. Srinivasa, S.R. Dharwadkar, Synthesis of $CaTiO3$ from calcium titanyl oxalate hexahydrate (CTO) as precursor employing microwave heating technique. Bull. Mater. Sci. **30**, 225–229 (2007)

35. P. Thiruramanathan, A. Marikani, D. Madhavan, S. Bharadwaj, A.M. Awasthi, Influence of calcination temperature on sol–gel synthesized single-phase bismuth titanate for high dielectric capacitor applications. Int. J. Mater. Res. **107**, 484–492 (2016)

36. Ranjit Kumar, M. Zulfequar, T. D. Senguttuvan, Improved giant dielectric properties in microwave flash combustion derived and microwave sintered $CaCu_3Ti_4O_{12}$ ceramics, J. Electroceram. **42**, 41–46 (2019).

37. L. Singh, K.D. Mandal, U.S. Rai, A.K. Rai, Effect of site selection on dielectric properties of Fe doped $CaCu_3Ti_4O_{12}$ electro-ceramic synthesized by citrate nitrate gel route. Indian J. Phys. **88**, 665–670 (2014)

38. E.C. Hunter, P.D. Battle, R. Paria Sena, J. Hadermann, Ferrimagnetism as a consequence of cation ordering in the perovskite $LaSr_2Cr_2SbO_9$, J. Solid State Chem. **248**, 96–103 (2017).

39. P. Thomas, K. Dwarakanath, K.B.R. Varma, T.R.N. Kutty, Nanoparticles of the giant dielectric material, $CaCu_3Ti_4O_{12}$ from a precursor route. J. Phys. Chem. Solids **69**, 2594–2604 (2008)

40. H. Ben Yahia, U.C. Rodewald, C. Feldmann, M. Roming, F. Weill, R. Pöttgen, X-Ray diffraction and SAED characterisations of $RE_4O_4[PO_4]Cl$ (RE = La, Pr, and Nd) and photoluminescence properties of Eu^{3+}-doped $La4O_4[PO_4]Cl$, J. Mater. Chem. C **2**, 1131- 1140 (2014).

41. M. Bahout, S.S. Pramana, J.M. Hanlon, V. Dorcet, R.I. Smith, S. Paofai, S.J. Skinner, Stability of $NdBaCo_{2−x}Mn_xO_{5+\delta}$ (x = 0, 0.5) layered perovskites under humid conditions investigated by high-temperature in situ neutron powder diffraction. J. Mater. Chem. A **3**, 15420–15431 (2015)

42. J. Tauc, A. Menth, States in the gap. J. Non-Cryst. Solids **8**, 569–585 (1972)

43. J.-W. Jeon, D.-W. Jeon, T. Sahoo, M. Kim, J.-H. Baek, J.L. Hoffman, N.S. Kim, I.-H. Lee, Effect of annealing temperature on optical band-gap of amorphous indium zinc oxide film. J. Alloys Compd. **509**, 10062–10065 (2011)

44. R. Muccillo, J.R. Carmo, Electrical conductivity of $Ca_{1−x}Sr_xTi_{0.65}Fe_{0.35}O_{3−\delta}$, x = 0, 0.5 and 1, polycrystalline compounds in the 300–500K range. Mater. Res. Bull. **47**, 1204–1211 (2012)

45. A. Kumar, R.K. Dwivedi, V. Pal, Dielectric behavior and impedance spectroscopy of $Ba_{1-x}Bi_xTi_{1-x}Fe_xO_3$ system. Adv. Mat. Res. **585**, 190–194 (2012)

46. S. Nayak, B. Sahoo, T.K. Chaki, D. Khastgir, Facile preparation of uniform barium titanate (BaTiO3) multipods with high permittivity: impedance and temperature dependent dielectric behavior. RSC Adv **4**, 1212–1224 (2014)

47. A. Kumar, R.K. Dwivedi, V. Pal, Dielectric behavior and impedance spectroscopy of $Ba_{1-x}Bi_xTi_{1-x}Fe_xO_3$ system. Adv. Mater. Res. **585**, 190–194 (2012)

48. N. Lenin, K. Sakthipandi, R.R. Kanna, J. Rajesh, Effect of neodymium ion on the structural, electrical and magnetic properties of nanocrystalline nickel ferrites. Ceram. Int. **44**, 11562–11569 (2018)

49. C. Mu, H. Zhang, Y. He, P. Liu, Influence of temperature on dielectric properties of Fe-doped $CaCu_3Ti_4O_{12}$ ceramics. Physica B Condens. Matter **405**, 386–389 (2010)

50. A.K. Jonscher, The 'Universal'' dielectric response.' Nature **267**, 673–679 (1977)

51. I.G. Austin, N.F. Mott, Polarons in crystalline and non-crystalline material. Adv. Phy. **18**, 41–102 (1969)

52. L.A. Dunyushkina, V.P. Gorelov, High temperature electrical behavior of $CaTi_{1−x}Fe_xO_{3−\delta}$ (x = 0–0.5). Oxygen-ion, electronic and proton conductivity, Solid State Ion. 253,169–174 (2013).